

HDPV-SLAM: Hybrid Depth-augmented Panoramic Visual SLAM for Mobile Mapping System with Tilted LiDAR and Panoramic Visual Camera

Mostafa Ahmadi¹, Amin Alizadeh Naeini¹, Mohammad Moein Sheikholeslami¹, Zahra Arjmandi¹, Yujia Zhang¹, and Gunho Sohn^{1†}

Abstract—This paper proposes a novel visual simultaneous localization and mapping (SLAM) system called Hybrid Depth-augmented Panoramic Visual SLAM (HDPV-SLAM), that employs a panoramic camera and a tilted multi-beam LiDAR scanner to generate accurate and metrically-scaled trajectories. RGB-D SLAM was the design basis for HDPV-SLAM, which added depth information to visual features. It aims to solve the two major issues hindering the performance of similar SLAM systems. The first obstacle is the sparseness of LiDAR depth, which makes it difficult to correlate it with the extracted visual features of the RGB image. A deep learning-based depth estimation module for iteratively densifying sparse LiDAR depth was suggested to address this issue. The second issue pertains to the difficulties in depth association caused by a lack of horizontal overlap between the panoramic camera and the tilted LiDAR sensor. To surmount this difficulty, we present a hybrid depth association module that optimally combines depth information estimated by two independent procedures, feature-based triangulation and depth estimation. During a phase of feature tracking, this hybrid depth association module aims to maximize the use of more accurate depth information between the triangulated depth with visual features tracked and the deep learning-based corrected depth. We evaluated the efficacy of HDPV-SLAM using the 18.95 km-long York University and Teledyne Optech (YUTO) MMS dataset. The experimental results demonstrate that the two proposed modules contribute substantially to the performance of HDPV-SLAM, which surpasses that of the state-of-the-art (SOTA) SLAM systems.

I. INTRODUCTION

Recently, vehicle-mounted mobile mapping systems (MMSs) have emerged as the primary spatial imaging system for capturing high-resolution maps of urban environments. Most commercially-available MMSs combine georeferencing technology with precise, high-speed, long-range laser scanning and high-resolution imaging sensors. In [1], a comprehensive analysis of contemporary MMSs was presented. With the most recent MMS technology, it is now possible to collect enormous quantities of precise, location-based data for various purposes. This includes creating detailed maps suitable for autonomous vehicles and the use of these maps to generate large-scale 3D representations of entire cities [2].

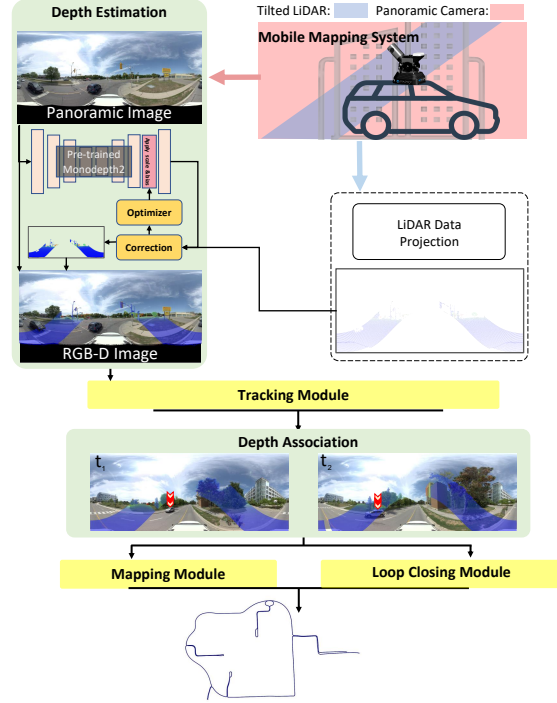


Fig. 1: A schematic workflow designed for HDPV-SLAM using MMS's panoramic camera and tilted LiDAR scanner. HDPV-SLAM proposes new modules including depth estimation and depth association (shown in green blocks).

However, the georeferencing capability of MMS significantly relies on advanced GNSS/IMU technology. The primary purposes of spatial imaging sensors such as cameras and LiDAR are to generate photorealistic textures and metrically-scaled depths. In GNSS-unfavorable environments, such as urban canyons and tunnels, MMS georeferences spatial data with limitations. In addition, we have recently observed a high demand for compact and inexpensive MMS designs to reduce system complexity, including using GNSS/IMU less frequently or not at all [1].

This investigation has two primary objectives. The first objective is to incorporate a mapping-capable MMS with a SLAM system. The MMS we utilized was equipped with a panoramic camera along with a tilted LiDAR, which is usually employed for road inspection or mapping. The second objective is to construct a metrically-scaled, accurate SLAM

[†]Corresponding author

¹The authors are with the Department of Earth and Space Science and Engineering, Lassonde School of Engineering, York University, 4700 Keele Street, Toronto, Ontario M3J 1P3, Canada. ahmadism@yorku.ca, naeini@yorku.ca, mmoein@yorku.ca, zahraarj@yorku.com, zhang89@yorku.ca, gsohn@yorku.ca

system that could operate in GPS-denied environments without the costly IMU sensor. SLAM systems are constrained by GPS limitations on use in such environments, and while high-end IMU sensors can circumvent this obstacle, they may be too costly for low-budget users. To address this issue, we conducted tests to ascertain the performance precision of inexpensive visual sensors in a boundary test scenario.

Our foundational work, RPV-SLAM [3], traverses the path to attaining the stated objectives but has certain limitations. RPV-SLAM is a keyframe-based RGB-D SLAM that generates metrically-scaled trajectories with comparatively small errors using only LiDAR along with a panoramic camera. According to the method, the depth channel of its RGB-D images is supplied by a LiDAR sensor. However, there are two restrictions in RPV-SLAM. First, it uses a simplistic bi-interpolation for LiDAR densification which disregards the scene's context and semantics that could be inferred from the corresponding imagery. Second, as a keyframe-based SLAM, RPV-SLAM generates 3D map points only with the keyframes using two independent modes of depth association, one powered by visual-feature-based triangulation and the other by LiDAR. Due to the significant disparity between the horizontal field of view provided by the panoramic camera and the tilted LiDAR scanner, multi-modal depth generation is required. Thus, the quality of map points generated by multi-modal depth generation varies depending on the ad hoc positioning of extracted features in the keyframes.

To address these issues, we propose HDPV-SLAM system, which employs two novel modules to enhance the precision of MMS's pose estimation. In HDPV-SLAM pipeline, we designed a deep-learning (DL)-based depth estimation module to resolve the limitations caused by the naive bi-interpolation for densifying the depth from the MMS's panoramic camera and tilted LiDAR sensor. DL-based depth estimation has shown a high level of proficiency in providing semantic-centric depth information to enhance the visual SLAM's performance [4]. However, the lack of real, depth-annotated datasets and the constantly-changing environment of SLAM systems, such as different lighting and weather conditions, hinder the generalization of deep depth estimation networks. This results in a subpar performance in practice and during the inference phase for complicated or unseen inputs. Using supervised and unsupervised approaches [5, 6], various adaptation methods attempt to alleviate this problem. For instance, DARS [7] is designed to use a pre-trained depth estimation network in conjunction with available sparse LiDAR points during inference and to adapt the network to each new input. Although DARS can provide us with a more precise and dense depth estimation, it was designed for perspective images, whereas the images in our problem have a panoramic geometry. In this study, we propose Panoramic Double-stage Adaptive Refinement Scheme (PanoDARS), an extension of DARS for panoramic images that generates DL-based depth estimation results approximated to LiDAR depth during the inference phase.

To circumvent the second limitation of RPV-SLAM, we

propose a depth association module that combines keyframe and non-keyframe frame (or non-keyframe for simplicity) depth information. Because our tilted LiDAR sensor has a small overlap region with the panoramic camera, two distinct depth generation procedures are carried out. First, generate 3D map points with keyframes using DL-based depth estimation if visual features are found in the overlapping region. Second, perform visual feature-based triangulation outside the overlapping region. Two distinct sensing mechanisms generate map points with varying degrees of precision. In our proposed depth association module, we cross-validate the accuracy of the single modal map point creation with the dual modalities and, if necessary, update the position of the associated map point with depth information from non-keyframes. This cross-validation task is accomplished by extending the depth association's capacity with non-keyframes, allowing visual feature-only map points to be tracked and compared with LiDAR-only map points located in an overlapping region. This cross-validation of multi-modal depth estimation results can enhance the positional accuracy of map points and maximize the use of available depth information from the LiDAR sensor.

In this study, we consider HDPV-SLAM's major contributions as follows:

- We propose a novel DL-based depth estimation module for iteratively densifying sparse LiDAR depth using panoramic images and LiDAR point clouds to improve the quality of depth estimation on visual features.
- We propose a novel hybrid depth association module that optimally combines depth information driven by triangulating visual features and LiDAR depth to address a problem caused by the lack of substantial spatial overlap between the panoramic camera and the tilted LiDAR sensor.

We review related works in Section II. The proposed HDPV-SLAM system is presented in Section III, and experimental results are discussed in Section IV. Finally, we present the concluding remarks on our work in Section V.

II. RELATED WORKS

A. Visual SLAM

In recent years visual SLAM and odometry have had various remarkable works, including ORB-SLAM [8], LSD-SLAM [9], DSO [10], and SVO [11]. The SOTA visual SLAM can be classified into filter-based SLAM and keyframe-based SLAM. MonoSLAM [12] is one of the filter-based methods that use the extended Kalman filter (EKF). In contrast, keyframe-based visual SLAM only utilizes selected frames known as keyframes for mapping instead of processing all frames, while non-keyframes are utilized for tracking purposes. Keyframes are also used in the loop closing module which detects the revisited keyframes and improves the performance of bundle adjustment optimization for large-scale environments. [13] presents a literature review on keyframe-based SLAM systems.

B. RGB-D SLAM

RGB-D SLAMs have gained considerable attention in the literature due to their high accuracy and are being widely used in real-world applications. These methods are a type of visual SLAM that have been proposed for RGB-D cameras and their trend mostly follows the monocular methods. Just like the monocular visual SLAMs, RGB-D SLAMs can be categorized into feature-based and direct methods. Feature-based methods like [8, 14] extract features from the image and use the geometry of the reconstructed scene for the camera pose estimation. Although these methods fail in certain environments where their feature extractor fails, they are computationally efficient compared with the direct methods. However, direct methods like [15, 16], on the other hand, utilize the whole RGB-D image to minimize the photometric error between the predicted image and the observed image. But the big downside of these methods is that they are more computationally expensive.

C. Metrically-scaled SLAM

To solve the scale ambiguity problem of visual SLAM results, a diverse range of methods have been suggested so far, and it is quite an old topic in the literature. Some propose the usage of auxiliary sensors. For example, [17] uses GPS data, and [18] uses ground control points; both have limited use cases. In contrast, PIW-SLAM [19] generates metrically-scaled results with the help of IMU and wheel encoder, which does not limit the SLAM for real-world applications. Furthermore, the works of [20, 21] use RGB-D cameras like Kinect providing aligned dense depth data for monocular images.

In the context of solving the ambiguity problem, the utilization of RGB-D-like images has been efforts, too. [22] utilizes a deep neural network to predict a depth image for each frame and have it as the D channel in RGB-D images for the input of their RGB-D SLAM. Similar to the previous work, [23] proposes the usage of deep convolutional neural fields for depth estimation. RPV-SLAM [3] uses a sparse LiDAR sensor and using the bi-interpolation of the LiDAR points, forms the D channel of the input RGB-D image along with the panoramic RGB image. Although usage of a LiDAR sensor with a pinhole camera in the SLAM community has been addressed and has proven its strengths [24], utilizing a LiDAR sensor with a panoramic camera has been an undervalued topic, and to the best of our knowledge RPV-SLAM is the only one.

D. Depth Estimation

Depth estimation is called to the process of estimating depth for input RGB images. Recently, It has become a hot topic due to the success of deep learning methods [25, 26] and its various applications ranging from 3D reconstruction [27] to autonomous vehicles [28]. RGB-D SLAM often suffers from sparse depth measurements and depth estimation suffers from scale ambiguity and lack of ground truth data, so these two tasks can contribute to each other [29]. In this sense, a number of works have tried improving the

performance of depth estimation [30], SLAM [4] or even both [31] through a complementary design.

Unlike the tremendous research on perspective depth estimation, considerably fewer studies have been dedicated to panoramic depth estimation. One main reason for that is the lack of appropriate panoramic datasets for depth estimation [32]. Therefore, some research such as [33] suggest training existent networks on synthetic panoramic images. Another approach is domain adaptation from perspective to panoramic. For instance, [34] takes the available pre-trained networks on perspective images and replaces the standard convolutions with a distortion-aware version of convolutions to infer on panoramic images. OmniFusion [35] also transforms panoramic images into perspective images, then estimates the depth and eventually merges them to reconstruct the panoramic depth. As another approach, [32] advocates self-supervised learning to eliminate the need for panoramic depth data during training. Furthermore, it is worth mentioning that, among all the above approaches, adaptation of perspective models to the panoramic domain apparently has gained increasing attention as a practical solution in other tasks as well [36, 37].

III. HYBRID DEPTH-AUGMENTED PANORAMIC VISUAL SLAM

As shown in Figure 2, HDPV-SLAM includes modules for depth estimation, depth association, tracking, mapping, and loop closing modules. This section describes each module in detail.

A. SLAM Input

In the first stage, an RGB-D image is created by combining a panoramic RGB image and its corresponding LiDAR point cloud. The image channel D is created by projecting LiDAR data onto the image plane. Using calibration parameters between the camera and the LiDAR sensor, this task is completed in accordance with the prior work [3].

Then, for each RGB-D image in the capturing order, frame F_t is created, where $t \in \{1, 2, 3, \dots, n\}$ and n is the total number of RGB-D images. \mathbf{F} is the array of all frames. Each $F_t \in \mathbf{F}$ contains RGB image $\mathbf{I}_t \in \mathbb{R}^{w \times h \times 3}$ of the width w and the height h and a corresponding projected sparse LiDAR $\mathbf{D}_t^s \in \mathbb{R}^{w \times h}$. In Section III-B, we describe a method to densify \mathbf{D}_t^s and get $\hat{\mathbf{D}}_t \in \mathbb{R}^{w \times h}$. Also, a frame F_t contains O_t which is the array of the ORB features extracted from \mathbf{I}_t using the ORB feature extractor. For each $o_t^i \in O_t$ we have $o_t^i \in \{(u, v) | u, v \in \mathbb{W}, 0 \leq u < w, 0 \leq v < h\}$ where $i \in \{1, 2, 3, \dots, m_t\}$ and m_t is the total number of ORB features of I_t .

The output of the SLAM system is the array of all the camera positions J and the set of all the map points ρ . Each $j_t \in \mathbb{R}^3 \times SO(3)$ in J is the position and the orientation of the camera at time t in world coordinate, and each $p \in \mathbb{R}^3$ in ρ shows the position of a map point in the world coordinate. We define subsets of ρ , for each t as we create map points using F_t . The relation between ρ_t for different t is $\{\} = \rho_0 \subseteq \rho_1 \subseteq \rho_2 \subseteq \dots \rho_{n-1} \subseteq \rho_n = \rho$. Each $\rho_t \subseteq \rho$ is updated

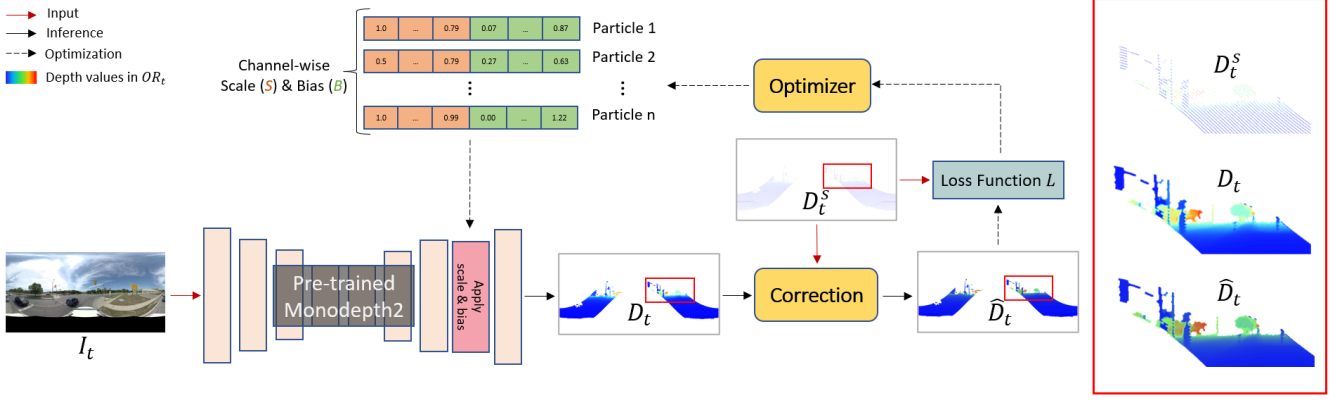


Fig. 2: A schematic architecture designed for the depth estimation module, called PanoDARS. PanoDARS uses panoramic imagery as a primary source for predicting the depths to generate RGB-D images, while LiDAR data is used as supplementary information to correct the predicted depth. A pre-trained network predicts a depth image \mathbf{D}_t using panoramic imagery as primary source. Given a sparse depth \mathbf{D}_t^s , the predicted \mathbf{D}_t is adjusted to the acquired LiDAR point clouds for generating a corrected depth $\hat{\mathbf{D}}_t$. Finally, a refined dense depth is generated by optimizing embedded feature space to minimize the loss between \mathbf{D}_t^s and $\hat{\mathbf{D}}_t$ in an iterative manner during the inference phase.

with the new map points created from F_t each time a new frame F_t comes in. And when $t = n$, we have $\rho_t = \rho$

B. Depth Estimation Module

The depth estimation module aims to produce a dense depth map $\hat{\mathbf{D}}_t$ by taking an input RGB image \mathbf{I}_t at the time t and a corresponding sparse LiDAR \mathbf{D}_t^s . This module enables increasing the number of ORB visual features augmented with depth in the overlapping region (OR_t) between the panoramic imagery and the LiDAR point clouds. To do this, a new version of DARS [7] for panoramic depth estimation, called PanoDARS, is proposed (see Figure 2). DARS [7] was originally designed for adaptive depth refinement on perspective images, while PanoDARS has to adapt the models pre-trained on perspective images to panoramic ones. However, depth estimation on panoramic images presents some obstacles. First, because there is no publicly accessible standard dataset for panoramic depth estimation, supervised models cannot be used. Second, self-supervised methods must be improved by non-metrically scaled estimations and are notably difficult for panoramic geometry. Thus, the suggested solution is to adapt a pre-trained depth estimation baseline over perspective images to our panoramic dataset.

PanoDARS consists of two stages, correction and optimization. In [7], the depth maps are divided into three horizontal slices, with the correction values in each slice being independently calculated. Since LiDAR sparsity patterns differ between panoramic and perspective geometries, the proposed method omits slicing during the correction phase. Moreover, PanoDARS only estimates depth in I_t regions where sparse depth is available nearby (OR_t , as shown in the rainbow-colored image on the left of Figure 3).

In the first stage, a correction value $\delta d_t^s \in \Delta \mathbf{D}_t^s$ between each valid pixel in the sparse depth map $d_t^s \in \mathbf{D}_t^s$ and its correspondence $d_t \in \mathbf{D}_t$ is calculated using $\delta d_t^s = d_t - d_t^s$.

Then, an interpolation function $Q : \mathbb{R}^2 \mapsto \mathbb{R}$ based on Delaunay triangulation [38] is leveraged to obtain a dense correction map $\Delta \mathbf{D}_t = Q(\Delta \mathbf{D}_t^s)$. Finally, the corrected depth map $\hat{\mathbf{D}}_t = \mathbf{D}_t + \Delta \mathbf{D}_t$ is calculated. $\hat{\mathbf{D}}_t$ is a sufficiently accurate initial value for the second stage.

In the second stage, while the pre-trained weights are fixed, some learnable auxiliary parameters are applied to intermediate features in the baseline. By optimizing those parameters, the predicted depth is refined. Therefore, the overall performance of PanoDARS is as follows.

Given an input RGB image $\mathbf{I}_t \in \mathbb{R}^{w \times h \times 3}$, PanoDARS splits the pre-trained baseline $M : \mathbb{R}^{w \times h \times 3} \mapsto \mathbb{R}^{w \times h}$ into a body $G : \mathbb{R}^{w \times h \times 3} \mapsto \mathbb{R}^{a \times b \times c}$ and a head $H : \mathbb{R}^{a \times b \times c} \mapsto \mathbb{R}^{w \times h}$, where a , b , and c are respectively width, height, and number of channels of the intermediate feature set $G(\mathbf{I}_t) \in \mathbb{R}^{a \times b \times c}$. The auxiliary parameters, scales $\mathbf{S} \in \mathbb{R}^c$ and biases $\mathbf{B} \in \mathbb{R}^c$ are applied on $G(\mathbf{I}_t)$, and the depth $\mathbf{D}_t = H(\mathbf{S} \otimes G(\mathbf{I}_t) \oplus \mathbf{B})$ is predicted, where \otimes and \oplus represent channel-wise multiplication and addition. Afterwards, the correction module $C : \mathbb{R}^{w \times h} \mapsto \mathbb{R}^{w \times h}$ carries out the first refinement stage on \mathbf{D}_t and returns $\hat{\mathbf{D}}_t = C(\mathbf{D}_t, \mathbf{D}_t^s)$.

The auxiliary parameters $\mathbf{X} \in \mathbb{R}^{2c}$, i.e., concatenated channel-wise scales (\mathbf{S}) and biases (\mathbf{B}), are learnable. Therefore, the following optimization problem can be formulated as $L(\hat{\mathbf{D}}_t(\mathbf{I}_t, \mathbf{X} + \Delta \mathbf{X}), \mathbf{D}_t^s) \rightarrow \min_{\Delta \mathbf{X}}$.

where $\Delta \mathbf{X}$ is the corrections applied on the parameters and L is the cost function given to particle swarm optimizer (PSO) [39]. Hence, the second stage of refinement is conducted by PSO.

C. Tracking Module

The tracking module establishes relationships between extracted visual features and existing map points. The tracking module accepts an input of F_t for each t in sequential order at the start of a SLAM run. The matching process within

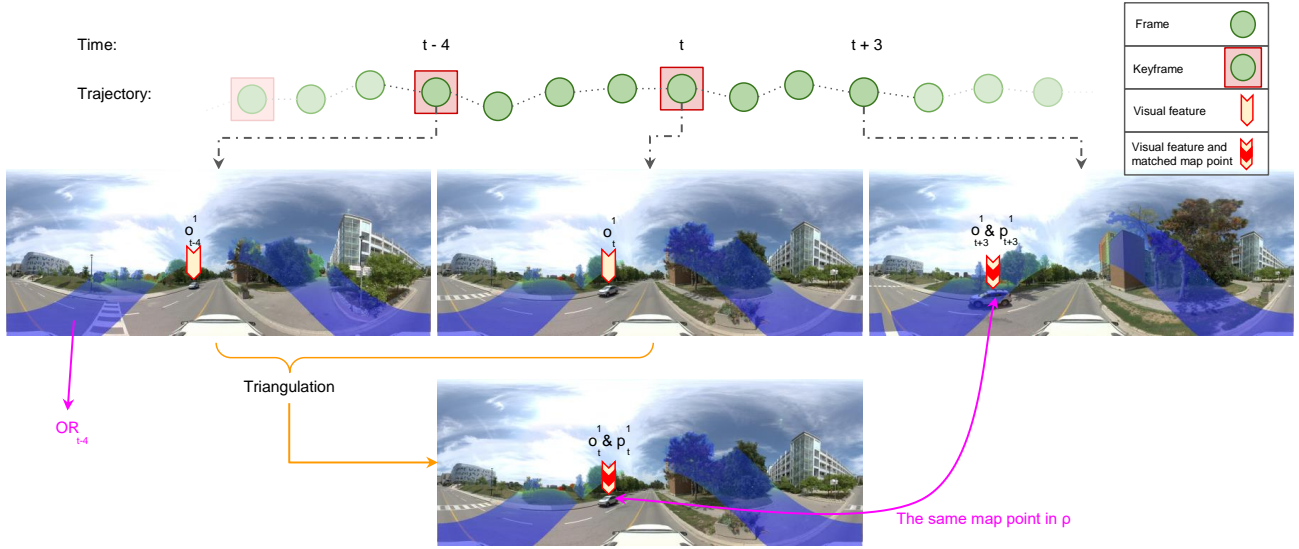


Fig. 3: A map point p_t^1 is created at time t by triangulating visual features of times $t-4$ and t . This triangulation is because these two visual features are not in OR_{t-4} and OR_t . In F_{t+3} , o_{t+3}^1 points to the middle of the parked car's rooftop and matches with the previously created p_t^1 at time t which is now called p_{t+3}^1 . At time $t+3$, o_{t+3}^1 is inside OR_{t+3} , which means the depth data is available. This enables the system to estimate the map points' 3D position more precisely through the depth coming from the depth estimation method.

the tracking module will locate matches between ρ_{t-1} and generate an array of matched map points P_t and O_t . P_t has the same size as O_t (which is m_t) and can also contain *Null* values at certain indices. For each matched pair of o_t^i and a map point from ρ_{t-1} , P_t contains a p_t^i pointing to the map point. $p_t^i = \text{Null}$ if o_t^i does not match any map point from ρ_{t-1} . The tracking module can estimate j_t based on these local matches. The system then designates a frame F_t as a keyframe when it determines that the tracking will perform poorly in the future with estimates of j_t based on a limited number of map points.

D. Mapping Module

When the tracking module decides F_t to be a keyframe, the mapping module creates new map points using F_t and puts them together with ρ_{t-1} to save all of them in ρ_t . The module attempts to create a map point for each o_t^i that its corresponding p_t^i is *Null*. If $o_t^i \in OR_t$, it creates a map point using o_t^i , j_t , and $\hat{D}_t(o_t^i)$. If $o_t^i \notin OR_t$, it will triangulate F_t with the nearest neighboring keyframe F_s to estimate the depth for o_t^i and create the map point with the same set of information. If triangulation is not successful, the module will not create a map point for o_t^i . The mapping module is also responsible for local bundle adjustment, which is accomplished by following [3].

E. Depth Association Module

We propose a novel hybrid depth association module for associating optimal depth information with visual features in OR_t . After the tracking module has tracked all visible map points in the current frame F_t and estimated j_t , this depth association module is triggered. The proposed module is executed even if F_t is not a keyframe for augmenting O_t with

\hat{D}_t , unlike conventional methods. A key motivation for using non-keyframes in the depth association is to cross-validate the accuracy of tracked map points and update the map points by conducting the depth association optimally. As previously described, a map point can be generated using either the direct assignment of LiDAR-driven depth to a visual feature or the visual feature-based triangulation; it depends on the position of the corresponding feature in the image plane (i.e., being inside OR_t or out of it). Consequently, the depth value associated with a tracked map point may vary. The new method resolves this inconsistency issue by executing an optimal depth association task following established policies.

Algorithm 1 shows the suggested hybrid depth association process. It inputs F_t and the tracked array of map points P_t . For each i , if the matching module has not assigned any map points to o_t^i or if o_t^i is out of OR_t , it skips the i and goes for the next member of O_t . If o_t^i passes these conditions, then a $new p_t^i \in \mathbb{R}^3$ will be created using o_t^i , its depth value ($\hat{D}_t(o_t^i)$), and its depth value and the position and orientation of the camera at time t (j_t). But, sometimes the tracking module can make mistakes in assigning ORB visual features to the corresponding map points. So we have defined a rejection threshold θ (in meters) to prevent big mistakes and their effect on the whole trajectory. If the distance between the current position of p_t^i and the newly calculated $new p_t^i$ is bigger than θ , we will not change anything. If not, then we have defined two policies here:

- If p_t^i has been created using triangulation and not modified using any depth map later, the algorithm will change the location of p_t^i to $new p_t^i$.
- Or, if the depth value of the visual feature that previously has modified (or created) the position of p_t^i

$(\hat{\mathbf{D}}_p(o_t^i))$ is larger than the current depth $(\hat{\mathbf{D}}_t(o_t^i))$, again the algorithm will change the location of p_t^i to $new p_t^i$.

Figure 3 shows an example of this algorithm for the first policy with a simple scenario where we only have one ORB feature in each frame. And the second policy helps with the precise estimation of the position of the map points. Each time a map point is observed with a smaller depth value, the algorithm recalculates its position based on it.

Algorithm 1 Depth Association Module Algorithm

Input: Current frame F_t and the tracked array of map points P_t

- 1: $\theta \leftarrow$ The rejection threshold
- 2: **for** Each p_t^i in P_t **do**
- 3: **if** $p_t^i = \text{Null}$ or $o_t^i \notin OR_t$ **then**
- 4: **continue**
- 5: **end if**
- 6: $F_p \leftarrow$ Last keyframe who created or modified p_t^i
- 7: $new p_t^i \leftarrow$ Estimated 3D position using o_t^i , $\hat{\mathbf{D}}_t(o_t^i)$, and j_t
- 8: **if** $\text{distance}(p_t^i, new p_t^i) < \theta$ **then**
- 9: **if** (p_t^i created using triangulation and not modified after that) or $(\hat{\mathbf{D}}_t(o_t^i) < \hat{\mathbf{D}}_p(o_t^i))$ **then**
- 10: p_t^i 's position $\leftarrow new p_t^i$
- 11: Update p_t^i in P_t and all the previous subsets
- 12: **end if**
- 13: **end if**
- 14: **end for**

F. Loop Closing Module

Finally, after the loop closing module detects a loop, it performs the global bundle adjustment on the trajectory inside the loop. The global bundle adjustment performs a pose-graph optimization on j_t of the camera in each $F_t \in \{\text{the subset of keyframes in the loop}\}$. And also it optimizes all of the map points created in those keyframes. For the pose-graph optimization, we have used a similarity transformation.

IV. EXPERIMENTAL RESULTS AND DISCUSSION

This section comprises experimental analyses that examine the individual and combined performance of two modules through an ablation study. Additionally, we assess the performance of the most effective method with the combination of two modules identified in the ablation study on the entire dataset. We used York University and Teledyne Optech (YUTO) MMS dataset. The dataset has been acquired by Teledyne Optech's Maverick MMS with four sequences in various outdoor environments with an 18.95 km long road in York University's Keele Campus to test different urban situations. The characteristic details of the dataset can be found in the reference [3].

A. SLAM Trajectory Results

First, an ablation study was conducted on Sequence B of the dataset (see Table I). Then, the proposed method was compared with the competing methods, i.e., Google Cartographer [40] and RPV-SLAM [3] (see Table II). For all of the comparisons, we have used absolute trajectory error (ATE) [41], relative trajectory error (RTE) [42], and relative rotation error (RRE). For RRE and RTE, we have averaged

these measurements over sub-trajectories with a length of 100, 200, ..., and 800m.

The ablation study aims to find the optimum value for θ in Algorithm 1 and also to evaluate the effectiveness of depth association and depth estimation modules. Bi-interpolation described in [3] has been used as a rival to the depth estimation module.

According to Table I, in the absence of the depth association module, i.e., the first three rows, RPV-SLAM and the proposed method show similar performance in terms of both ATE and RTE, yet significantly better than Cartographer. Further, it proves that the bi-interpolation and the depth estimation module have no superiority over each other when there is no depth association module. On the other hand, considering different values of θ , bi-interpolation and depth estimation module illustrate a similar behavior, where increasing θ leads to worse ATE and RTE. Moreover, the best accuracy for both densification methods was obtained using $\theta = 2$.

As Table I suggests, when the depth association module was utilized (with θ), more accurate results were obtained. In addition, the depth estimation module outperforms bi-interpolation in both ATE and RTE, given identical values for θ . Regardless of selected depth densification methods, $\theta = 2$ shows the best performance in both ATE and RTE. In conclusion, we can attain the best performance when the depth estimation module and $\theta = 2$ are used. It means the depth estimation and depth association module have contributed to the improvement of the SLAM performance in both ATE and RTE.

Table II shows the results of our best setting (depth estimation module with $\theta = 2$) in comparison with Google Cartographer [40] and RPV-SLAM [3]. Google Cartographer is a LiDAR-centric SLAM that is also equipped with IMU. Overall, relatively poor results are obtained in residential areas due to unfavorable illumination conditions such as shadows. As expected, the parking lots sequence produced the best ATE performance because of its shorter length and lower scene complexity. Furthermore, the largest improvement in ATE was achieved in Sequence C due to the relatively shorter LiDAR ranges in residential areas.

To conclude, HDPV-SLAM produced the best results compared to Cartographer and RPV-SLAM over all the test sequences in terms of both ATE and RTE. Although the performance of HDPV-SLAM varies depending on the sequence, the other SLAM systems follow a similar pattern in their performances as well.

B. Discussion

As seen in Table I, the proposed technique outperforms the alternatives in terms of ATE. ATE is a metric that compares the entire trajectory to the ground truth and handles the form matching between them, indicating that the proposed method preserves the shape more effectively than the other methods. Furthermore, in three-quarters of the dataset, the RTE and RRE of the proposed technique are superior to those of the competing methods, and in one-quarter, they are second best

TABLE I: SLAM trajectory results for ablation study on Sequence B.

SLAM	Densification method	θ (m)	ATE (m)	RTE (%)	RRE ($^{\circ}$ /m)
Cartographer	N/A	N/A	142.97	16.57	0.0093
RPV-SLAM	bi-interpolation	N/A	12.91	1.51	0.0009
Proposed method	depth estimation module	N/A	12.95	1.64	0.0010
Proposed method	bi-interpolation	1	11.99	1.62	0.0009
Proposed method	bi-interpolation	2	9.93	1.43	0.0010
Proposed method	bi-interpolation	3	10.19	1.56	0.0009
Proposed method	bi-interpolation	4	13.01	1.63	0.0010
Proposed method	bi-interpolation	5	13.70	1.74	0.0010
Proposed method	depth estimation module	1	11.28	1.54	0.0009
Proposed method	depth estimation module	2	9.58	1.23	0.0011
Proposed method	depth estimation module	3	11.96	1.65	0.0009
Proposed method	depth estimation module	4	12.24	1.52	0.0010
Proposed method	depth estimation module	5	14.16	1.95	0.0010

TABLE II: SLAM trajectory results for all the sequences. Settings of HDPV-SLAM is based on Table I.

SLAM	Sequence	ATE (m)	RTE (%)	RRE ($^{\circ}$ /m)	SLAM	Sequence	ATE (m)	RTE (%)	RRE ($^{\circ}$ /m)
Cartographer	A	4.15	6.79	0.0507	C	A	180.95	5.78	0.0133
RPV-SLAM	A	1.62	3.25	0.0268	C	A	30.66	2.82	0.0042
Proposed method	A	1.40	3.59	0.0041	C	A	11.93	2.77	0.0034
Cartographer	B	142.97	16.57	0.0093	D	B	57.74	4.65	0.0137
RPV-SLAM	B	12.91	1.51	0.0009	D	B	5.67	1.49	0.0016
Proposed method	B	9.58	1.23	0.0011	D	B	4.69	0.9	0.001

by a slight margin. All of these comparisons demonstrate that the proposed strategy is superior.

V. CONCLUSIONS

In conclusion, we present the novel HDPV-SLAM system that uses a depth estimation module and a depth association module. The depth estimation module generates depth information for panoramic images adapting a perspective model as its baseline. Furthermore, the depth association module leverages all the possible DL-based depth information in keyframes and non-keyframes. However, the proposed method has some limitations as well. We noticed YUTO MMS dataset has dynamic scene objects like cars, buses, people, etc. The SLAM system suffers from these dynamic objects that degrade its performance. As a future work, the visual features coming from these dynamic objects can be filtered out to prevent errors. Another limitation is that the depth association module uses a rule-based algorithm for updating map points. For future investigations, semantic information can be utilized for more precise validation of the matched visual feature and map point pairs.

ACKNOWLEDGEMENT

This initiative, entitled "3D Mobile Mapping Using Artificial Intelligence," is funded by Teledyne Optech and the Natural Sciences and Engineering Research Council of Canada (NSERC) Collaborative Research Development (CRD).

REFERENCES

- [1] M. Elhashash, H. Albanwan, and R. Qin. "A Review of Mobile Mapping Systems: From Sensors to Applications". In: *Sensors* 22.11 (2022), p. 4262.
- [2] O. Al-Bayari. "Road Rehabilitation Using Mobile Mapping System and Building Information Model". In: (2019).
- [3] J. Kang et al. "RPV-SLAM: Range-augmented Panoramic Visual SLAM for Mobile Mapping System with Panoramic Camera and Tilted LiDAR". In: *2021 20th International Conference on Advanced Robotics (ICAR)*. IEEE. 2021, pp. 1066–1072.
- [4] K. Tateno et al. "Cnn-slam: Real-time dense monocular slam with learned depth prediction". In: *Proceedings of the IEEE conference on computer vision and pattern recognition*. 2017, pp. 6243–6252.
- [5] C. Zhao, Y. Tang, and Q. Sun. "Unsupervised monocular depth estimation in highly complex environments". In: *IEEE Transactions on Emerging Topics in Computational Intelligence* 6.5 (2022), pp. 1237–1246.
- [6] Y.-T. Yen et al. "3D-PL: Domain Adaptive Depth Estimation with 3D-Aware Pseudo-Labeling". In: *Computer Vision–ECCV 2022: 17th European Conference, Tel Aviv, Israel, October 23–27, 2022, Proceedings, Part XXVII*. Springer. 2022, pp. 710–728.
- [7] A. Alizadeh Naeini, M. M. Sheikhholeslami, and G. Sohn. "An Adaptive Refinement Scheme for Depth Estimation Networks". eng. In: *Sensors (Basel, Switzerland)* 22.24 (Dec. 2022), p. 9755. ISSN: 1424-8220. DOI: 10.3390/s22249755.
- [8] R. Mur-Artal and J. D. Tardós. "Orb-slam2: An open-source slam system for monocular, stereo, and rgbd cameras". In: *IEEE transactions on robotics* 33.5 (2017), pp. 1255–1262.
- [9] J. Engel, J. Stückler, and D. Cremers. "Large-scale direct SLAM with stereo cameras". In: *2015 IEEE/RSJ international conference on intelligent robots and systems (IROS)*. IEEE. 2015, pp. 1935–1942.
- [10] J. Engel, V. Koltun, and D. Cremers. "Direct sparse odometry". In: *IEEE transactions on pattern analysis and machine intelligence* 40.3 (2017), pp. 611–625.

[11] C. Forster, M. Pizzoli, and D. Scaramuzza. “SVO: Fast semi-direct monocular visual odometry”. In: *2014 IEEE international conference on robotics and automation (ICRA)*. IEEE. 2014, pp. 15–22.

[12] A. J. Davison et al. “MonoSLAM: Real-time single camera SLAM”. In: *IEEE transactions on pattern analysis and machine intelligence* 29.6 (2007), pp. 1052–1067.

[13] G. Younes et al. “Keyframe-based monocular SLAM: design, survey, and future directions”. In: *Robotics and Autonomous Systems* 98 (2017), pp. 67–88. ISSN: 0921-8890. DOI: <https://doi.org/10.1016/j.robot.2017.09.010>.

[14] Q. Li et al. “Point-line feature fusion based field real-time RGB-D SLAM”. In: *Computers & Graphics* 107 (2022), pp. 10–19. ISSN: 0097-8493. DOI: <https://doi.org/10.1016/j.cag.2022.06.013>.

[15] R. A. Newcombe, S. J. Lovegrove, and A. J. Davison. “DTAM: Dense tracking and mapping in real-time”. In: *2011 international conference on computer vision*. IEEE. 2011, pp. 2320–2327.

[16] T. Whelan et al. “ElasticFusion: Dense SLAM without a pose graph”. In: *Robotics: Science and Systems*. 2015.

[17] Y. Shi et al. “GPS-supported visual SLAM with a rigorous sensor model for a panoramic camera in outdoor environments”. In: *Sensors* 13.1 (2012), pp. 119–136.

[18] S. Ji et al. “Panoramic SLAM from a multiple fisheye camera rig”. In: *ISPRS Journal of Photogrammetry and Remote Sensing* 159 (2020), pp. 169–183.

[19] F. Jiang, J. Chen, and S. Ji. “Panoramic visual-inertial SLAM tightly coupled with a wheel encoder”. In: *ISPRS Journal of Photogrammetry and Remote Sensing* 182 (2021), pp. 96–111.

[20] C. Kerl, J. Sturm, and D. Cremers. “Robust odometry estimation for RGB-D cameras”. In: *2013 IEEE international conference on robotics and automation*. IEEE. 2013, pp. 3748–3754.

[21] J. Huai, Y. Zhang, and A. Yilmaz. “REAL-TIME LARGE SCALE 3D RECONSTRUCTION BY FUSING KINECT AND IMU DATA.” In: *ISPRS Annals of Photogrammetry, Remote Sensing & Spatial Information Sciences* 2 (2015).

[22] L. Tiwari et al. “Pseudo rgb-d for self-improving monocular slam and depth prediction”. In: *Computer Vision–ECCV 2020: 16th European Conference, Glasgow, UK, August 23–28, 2020, Proceedings, Part XI*. Springer. 2020, pp. 437–455.

[23] X. Yin et al. “Scale Recovery for Monocular Visual Odometry Using Depth Estimated with Deep Convolutional Neural Fields”. In: *2017 IEEE International Conference on Computer Vision (ICCV)*. 2017, pp. 5871–5879. DOI: [10.1109/ICCV.2017.625](https://doi.org/10.1109/ICCV.2017.625).

[24] C.-C. Chou and C.-F. Chou. “Efficient and Accurate Tightly-Coupled Visual-Lidar SLAM”. In: *IEEE Transactions on Intelligent Transportation Systems* (2021).

[25] S. F. Bhat, I. Alhashim, and P. Wonka. “Adabins: Depth estimation using adaptive bins”. In: *Proceedings of the IEEE/CVF Conference on Computer Vision and Pattern Recognition*. 2021, pp. 4009–4018.

[26] R. Ranftl, A. Bochkovskiy, and V. Koltun. “Vision transformers for dense prediction”. In: *Proceedings of the IEEE/CVF International Conference on Computer Vision*. 2021, pp. 12179–12188.

[27] C. Zhuang et al. “ACDNet: Adaptively combined dilated convolution for monocular panorama depth estimation”. In: *Proceedings of the AAAI Conference on Artificial Intelligence*. Vol. 36. 3. 2022, pp. 3653–3661.

[28] M. Fonder, D. Ernst, and M. Van Droogenbroeck. “M4Depth: Monocular depth estimation for autonomous vehicles in unseen environments”. In: *arXiv preprint arXiv:2105.09847* (2021).

[29] Y. Jin et al. “A Mono SLAM Method Based on Depth Estimation by DenseNet-CNN”. In: *IEEE Sensors Journal* 22.3 (2021), pp. 2447–2455.

[30] K. Sartipi et al. “Deep depth estimation from visual-inertial slam”. In: *2020 IEEE/RSJ International Conference on Intelligent Robots and Systems (IROS)*. IEEE. 2020, pp. 10038–10045.

[31] S. Y. Loo et al. “Online Mutual Adaptation of Deep Depth Prediction and Visual SLAM”. In: *arXiv preprint arXiv:2111.04096* (2021).

[32] I. Yun, H.-J. Lee, and C. E. Rhee. “Improving 360 monocular depth estimation via non-local dense prediction transformer and joint supervised and self-supervised learning”. In: *Proceedings of the AAAI Conference on Artificial Intelligence*. Vol. 36. 3. 2022, pp. 3224–3233.

[33] G. P. de La Garanderie, A. A. Abarghouei, and T. P. Breckon. “Eliminating the blind spot: Adapting 3d object detection and monocular depth estimation to 360 panoramic imagery”. In: *Proceedings of the European Conference on Computer Vision (ECCV)*. 2018, pp. 789–807.

[34] K. Tateno, N. Navab, and F. Tombari. “Distortion-aware convolutional filters for dense prediction in panoramic images”. In: *Proceedings of the European Conference on Computer Vision (ECCV)*. 2018, pp. 707–722.

[35] Y. Li et al. “Omnifusion: 360 monocular depth estimation via geometry-aware fusion”. In: *Proceedings of the IEEE/CVF Conference on Computer Vision and Pattern Recognition*. 2022, pp. 2801–2810.

[36] J. Zhang et al. “Bending reality: Distortion-aware transformers for adapting to panoramic semantic segmentation”. In: *Proceedings of the IEEE/CVF conference on computer vision and pattern recognition*. 2022, pp. 16917–16927.

[37] J. Zhang et al. “Transfer beyond the field of view: Dense panoramic semantic segmentation via unsupervised domain adaptation”. In: *IEEE Transactions on Intelligent Transportation Systems* 23.7 (2021), pp. 9478–9491.

[38] I. Amidror. “Scattered data interpolation methods for electronic imaging systems: a survey”. en. In: *Journal of Electronic Imaging* 11.2 (Apr. 2002), p. 157. ISSN: 1017-9909. DOI: [10.1117/1.1455013](https://doi.org/10.1117/1.1455013). URL: <http://electronicimaging.spiedigitallibrary.org/article.aspx?doi=10.1117/1.1455013> (visited on 01/02/2023).

[39] J. Kennedy and R. Eberhart. “Particle swarm optimization”. In: *Proceedings of ICNN’95 - International Conference on Neural Networks*. Vol. 4. Perth, WA, Australia: IEEE, 1995, pp. 1942–1948. ISBN: 9780780327689. DOI: [10.1109/ICNN.1995.488968](https://doi.org/10.1109/ICNN.1995.488968). URL: <http://ieeexplore.ieee.org/document/488968/> (visited on 01/02/2023).

[40] W. Hess et al. “Real-time loop closure in 2D LiDAR SLAM”. In: *2016 IEEE International Conference on Robotics and Automation (ICRA)*. Stockholm, Sweden: IEEE, May 2016, pp. 1271–1278. ISBN: 9781467380263. DOI: [10.1109/ICRA.2016.7487258](https://doi.org/10.1109/ICRA.2016.7487258). (Visited on 01/02/2023).

[41] J. Sturm et al. “A benchmark for the evaluation of RGB-D SLAM systems”. In: *2012 IEEE/RSJ International Conference on Intelligent Robots and Systems*. ISSN: 2153-0866. Oct. 2012, pp. 573–580. DOI: [10.1109/IROS.2012.6385773](https://doi.org/10.1109/IROS.2012.6385773).

[42] A. Geiger, P. Lenz, and R. Urtasun. “Are we ready for autonomous driving? The KITTI vision benchmark suite”. In: *2012 IEEE Conference on Computer Vision and Pattern Recognition*. ISSN: 1063-6919. June 2012, pp. 3354–3361. DOI: [10.1109/CVPR.2012.6248074](https://doi.org/10.1109/CVPR.2012.6248074).